

Self-aggregation conceptualized by cold pool organization

Silas Boye Nissen* and Jan O. Haerter†

*Niels Bohr Institute
University of Copenhagen
Blegdamsvej 17, 2100 Copenhagen
Denmark*

(Dated: August 3, 2022)

In radiative-convective equilibrium (RCE) simulations, self-aggregation is the spontaneous emergence of one or several long-lasting convective clusters from an apparently homogenous atmosphere [1]. This phenomenon may be implicated in the formation of tropical cyclones [2, 3] and large-scale events such as the Madden-Julian Oscillation [4–6]. However, it remains poorly understood how cold pools (CPs) contribute to self-aggregation. Using a suite of cloud-resolving numerical simulations, we link the life-cycle and the spatial organization of CPs to the evolution of self-aggregation. By tracking CPs, we determine the maximal CP radius $R_{\max} \approx 20$ km and show that cloud-free regions exceeding such radii always grow indefinitely. Besides, we identify a minimum CP radius $R_{\min} \approx 8$ km within which CPs are too negatively buoyant to initialize new convective cells. Finally, we suggest a simple mathematical framework describing the mechanism by which indefinitely growing cloud-free areas, termed *cavities*, form when CPs have small R_{\max} , whereas large R_{\max} hampers cavity formation. Our findings imply that interactions between CPs crucially control the dynamics of self-aggregation, and known feedbacks may only be required in stabilizing the final, fully-aggregated state.

I. SIGNIFICANCE STATEMENT

Convective self-aggregation describes the emergence of one or more persistently dry, cloud-free areas in numerical simulations and likely plays a key role in the formation of tropical cyclones and the Madden-Julian Oscillation. Some understanding of the clustering of thunderstorms in self-aggregation exists. However, how cold pools (CPs) contribute to this phenomenon remains poorly understood. CPs are radially expanding pockets of dense air that forms under precipitating thunderstorms. By analyzing cloud-resolving numerical simulations, we find that new convective events occur where two CPs collide. We find that the maximal radius that CPs achieve equals the minimum radius that allows cloud-free regions to persist. With this insight, we suggest that interactions between CPs control the appearance of self-aggregation.

II. INTRODUCTION

When rain evaporation is strong, so is the associated sub-cloud cooling and density increase [7, 8], forcing the resulting cold pools (CPs) to spread more quickly and cover larger areas [9–11]. Such pronounced CP activity has repeatedly been suggested to hamper convective self-aggregation in radiative-convective equilibrium (RCE) numerical experiments [12–15]. In these simulations, the atmosphere gradually organizes from an initial, apparently random, pattern of convective updraughts into an

inhomogeneous pattern with one or few strongly convecting patches, but an otherwise nearly precipitation-free domain [15–19]. A physical process commonly discussed as leading to self-aggregation is the positive feedback resulting from the altered radiation interaction with clouds and the associated modified atmospheric circulation when convective rain cells are organized. A circulation pattern builds up, where precipitating regions experience sustained long-level convergence. Surface latent and sensible heat fluxes — which increase under stronger surface wind speed — may further contribute.

Generically, the early stage of self-aggregation is characterized by the appearance of long-lived dry patches (termed *cavities* in the following), within which rain is suppressed [20]. Along with this suppression, further drying was reported to occur through radiative cooling and the resulting subsidence, as well as changes in surface fluxes. In this later stage, cavities expand and merge, eventually leaving only one contiguous moist region. A remarkable aspect of self-aggregation is hysteresis, by which it refuses to disaggregate, once formed, even when the initially required feedback is removed [13, 21, 22].

CPs are capable of mediating organization, as they effectively relay "information" between one precipitating cloud and its surroundings. Physically, CPs spread as density currents along the surface, carry kinetic energy and buoyancy, and can modify the thermodynamic structure of the environment near the CP edges [23–25]. CPs thereby act to pattern the convectively unstable atmosphere, as the loci where new convective cells emerge are not independent of the loci at which the previous cells dissipated. In particular, new cells were suggested to be spawned by the CP gust front alone, or by collisions between mobile gust fronts [25–27]. Inspired by the notion of CP interactions, conceptual work has formulated

* silas@nbi.ku.dk

† haerter@nbi.ku.dk

CPs as cellular automata [28, 29], and CP representations have been incorporated into large-scale models [30].

Here, we analyze a range of cloud-resolving simulations, which capture key processes at the CP gust fronts as well as their spreading and interaction (Fig. 1A–B, and *Materials and Methods*). By employing a CP tracking method [29], we follow the patterning of these CPs. Indeed, CPs predictably form a short time after rain falls through the boundary layer, and initially spread horizontally. CPs do not expand indefinitely but tend to stop growing near a radius of $R_{\max} \approx 20$ km, a value comparable to previous simulation results [9] and observational findings [31–33]. We discuss the formation and dynamics of cavities and the appearance of marked, non-random, line segments, which connect precipitation cell centers and are often nearly perfectly straight (Movie 1). To explain both features, we bring forward a simple model, based on the interaction of expanding circles, which mimics the collision of CP gust fronts and the resulting spawning of subsequent precipitation events.

III. RESULTS

We carried out $(960 \text{ km})^2$ simulations at 2 km horizontal resolution over idealized sea (termed *Sea2km*) and land surfaces (*Land2km*), as well as variants of both at higher grid resolution (*Sea400m* and *Land400m*) but smaller system sizes. Additionally, we employ data from a large domain, $(1024 \text{ km})^2$, and relatively high horizontal resolution (500 m, termed *Sea500m*), where the output time step was, however, limited due to data constraints (*Details: Methods*).

A. New cells formed in between cold pools

We begin by discussing *Sea2km*, where self-aggregation sets in after approximately seven days. When examining the simulation result after 20 days, we find that several large cavities without rainfall have emerged (Fig. 1A–B), and subsequently continue to grow — behavior typical of self-aggregation [15, 34]. In the humidity field, individual CPs and their gust fronts are easily distinguishable by the small and relatively dry areas (a few marked in Fig. 1A–B), which are separated by a network of positive humidity anomalies (yellow to red shades). Inspecting the pattern further, we find that new precipitation cells usually emerge close to the interfaces between the gust fronts from two distinct CPs (Fig. 1A).

The gust fronts have generally become immobile by the time a new precipitation event appears, but continue to generate positive water vapor anomalies due to persistent low-level circulations. Superimposing subsequent precipitation cells on the moisture field (small black patches), we find that a delay of typically 3–4 hours is required before any new cell emerges. At a subsequent time (Fig. 1B), the moisture field is modified due to the

action of previous rain cells (such as those marked in Fig. 1A). Locations with previous rain cells now are comparably dry, whereas their surroundings are again moistened. Tracking CP gust fronts by a tracer method [29] show that these gust fronts, emergent from each precipitation cell, tend to coincide with the positive moisture anomalies (several examples are highlighted in Fig. 1A–B). CP gust fronts hence concentrate moisture in between any two rain cells and excite new events at these locations [23].

When further inspecting the moisture field, it is apparent, that the strongest positive anomalies (red shades), tend to occur in between previous rain cells, but hardly ever at the edges of the large, dry cavities. We view this finding as evidence of rain cell-rain cell interactions, without which the formation of subsequent rain cells is unlikely. Given that the locations of newly emergent cells are systematically biased towards the collision lines formed by previous CP gust fronts, a systematic organizational pattern can be expected. In particular, a “filling-up,” by which CPs collide within a cavity, setting off a new rain cell there, should be unlikely for sufficiently large cavities. This is because CP gust fronts have a finite “reach,” that is, they do not exceed a certain radius. Therefore, they cannot spread across a large cavity.

B. Cavities need to reach a critical size before they grow indefinitely

Systematically tracking all CPs in *Sea2km*, we now study the life cycle of CPs after a given precipitation event initiates them. Similar to results reported elsewhere [33, 35, 36], CP gust fronts initially advance rapidly, but monotonically decrease their radial velocities (Fig. 1C). We contrast *Sea2km* to *Land2km*, where the latter mimics reduced surface latent heat fluxes (*Details: Methods*). We find that CPs are indeed limited in radius, but that those under drier conditions spread further, possibly due to reduced heating in their interior. To check for resolution sensitivity, we here also track CPs in *Sea400m* and *Land400m*, finding only weak resolution dependence of CP radii.

We now monitor the evolution of the large, longer-lived, cavities (such as those marked in Fig. 1A–B). We track all cavities emerging in *Sea500m*, *Sea2km*, and *Land2km* (*Details: Methods, Tracking of cavities*). An initial population of relatively small cavities is already present two days after the onset of precipitation (Fig. 1D–F and S2). When following the growth of these cavities, in *Sea500m* and *Sea2km*, some reach larger sizes and eventually contain coordinates that exceed distances $d > R_{\max}$ from any precipitation cell (red patches in Fig. 1D–E and Fig. S2). We refer to the value R_{\max} as a critical distance, as virtually any cavity of this size will continue to grow indefinitely (Fig. 1F). Cavities for which all points lie below the threshold R_{\max} may, however, decay in area. Long-tailed cavity area distributions

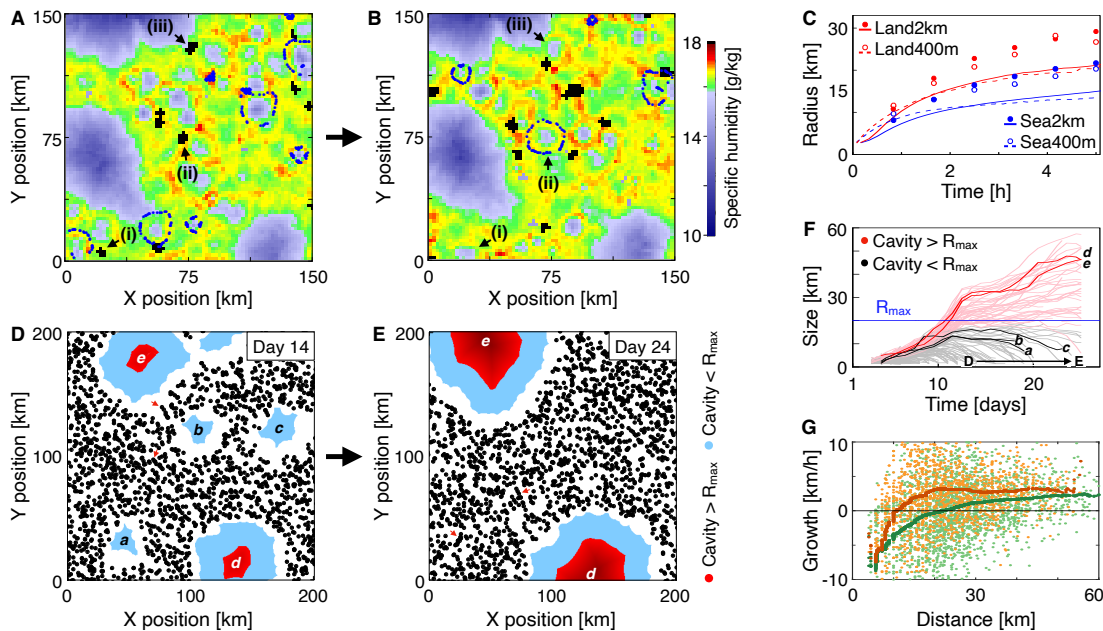


FIG. 1. **Cavities need to reach a critical size before they grow indefinitely.** (A) Specific humidity in the lowest model level ($z = 50$ m) at $t_1 = 17.49$ days (see color bar for units). Black blobs indicate rainfall patches that occurred at $t_1 + 4$ hours. Blue symbols indicate examples of tracked cold pool (CP) gust fronts, which were tracked by assigning tracers to the outer boundary of each rain patch and allowing these tracers to advect with the horizontal wind field (*Details: Methods*). Note the marked moisture enhancement near the CP gust fronts and that subsequent rain events are often set off near these areas of elevated moisture. (B) Analogous to (A), but at $t_2 = t_1 + 5.3$ h. Note that each rain event, indicated in (A), has left a distinct dry area behind. (C) CP growth is initially fast but monotonically slows over time. Symbols show the 90th percentile. (D–E) Five cavities (patches labeled a–e) identified in *Sea500m* where black dots are the CP centers. Blue regions are less than $R_{max} = 20$ km away from a CP center, and red regions are further away. (D) CP centers on day 14 and (E) day 24. Further days are shown in Fig. S2. Between day 14 and day 24, cavities with white labels (a–b) grow while cavities with black labels (c–e) shrink. Red arrows mark several line-like structures (see also Fig. 2). (F) The size evolution of all cavities identified. Black and gray cavities do not reach the critical size, R_{max} , whereas red cavities do. The five cavities in panel D–E are highlighted with lowercase letters, while uppercase letters highlight the timing of panels D and E, respectively. (G) The growth rate of all cavities in *Sea500m* (green) and *Sea2km* (red) as a function of size. The horizontal axis indicates the steady-state, whereas the solid curves are the average for a given size.

support the “rich-get-richer” dynamics (Fig. S4). Unbounded growth of some cavities causes merging events to take place, whereby multiple cavities connect to form even-larger ones — which eventually should lead to a fully-aggregated state.

Furthermore, by analyzing the growth rate of all cavities, we find that small cavities ($R_{max} < 20$ km) tend to shrink, whereas larger ones tend to grow (Fig. 1G). On average, we find the critical size in *Sea2km* to be lower than the critical size in *Sea500m*. We interpret this as a higher resolution simulation providing more violent CP interactions and more intense updrafts at the gust fronts and hence a higher triggering probability. The finding of higher resolution hampering self-aggregation is in line with sensitivity studies [12]. We bolster this explanation by examining updraft speeds for our simulations of different resolutions (4 km compared to 2 km, Fig. S3). We indeed find that updraft speeds can be much larger for the higher resolution, especially near CP gust fronts.

In *Land2km*, cavities generally remain far below R_{max} , and no cavities are formed that exist for more than one

day. Considering the CP radii again for *Land2km*, significantly larger distances can be covered, before CPs cease from growing — a finding that can explain the lack of cavity formation in *Land2km*.

C. Transient line segments emerge in simulation data

If CP interactions are relevant, as we claim, this should show in details of the spatial pattern formed. Therefore, we now characterize the spatial organization further: we connect the centers of all CPs present in a certain time window by the *line-of-sight* graph, also known as a Gabriel graph (dotted gray lines in Fig. 2A–B) [37]. Two CPs are line-of-sight neighbors if no other CPs are closer to the midpoint between the two CPs in question (Fig. S1). Analytically, we show that for a random seeding of positions, each CP center will, on average, have four neighbors within the line-of-sight (*Details: Supplementary Information*), and confirm this finding by nu-

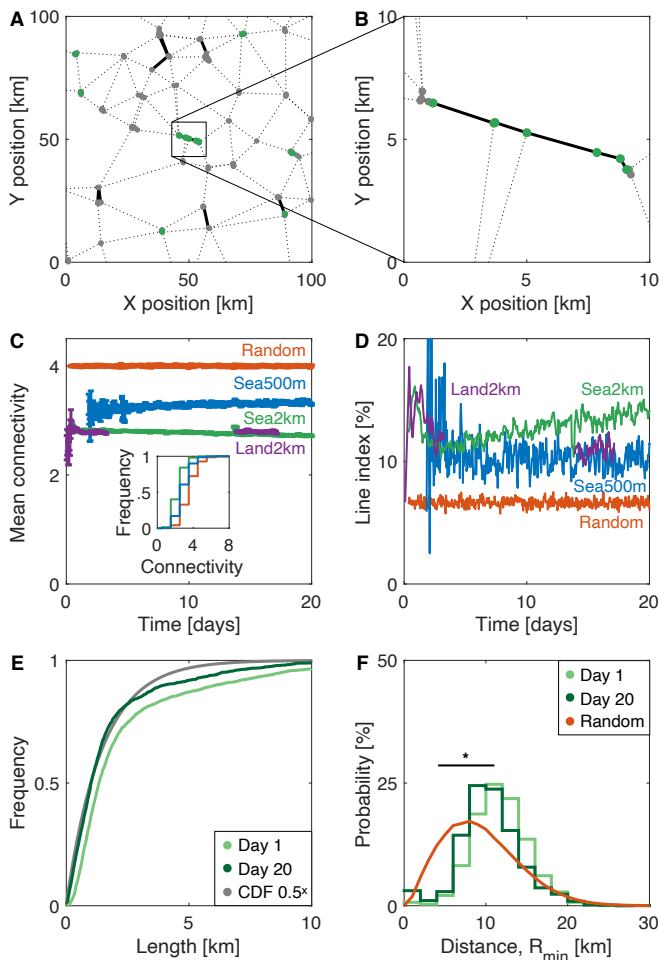


FIG. 2. Transient line segments emerge in simulation data. (A) A subset of *Sea2km* cold pool (CP) centers on day 10. Line-of-sight connections (gray dashed lines) that are shorter than $l = \sqrt{1/N}$ are marked as black lines. Within these, only those CPs with them and their neighbors having connectivity 2 counts towards the line index (green nodes). (B) Close-up of the line in (A). (C) The average line-of-sight connectivity is significantly lower in the simulation data (blue, green, and purple) compared to a randomized control (red). The standard error of the mean (SEM) is smaller than the thickness of the lines. The inset shows the accumulated frequency of the number of connections in *Sea500m* (blue) and *Sea2km* (green) relative to the control (red) on day 10. (D) The line index of simulation data (blue, green, and purple) is higher than the control, which has a line index of 6.6 ± 0.3 (red). (E) The cumulative distribution function (CDF) of line lengths at early and late times of *Sea2km*. The gray line is 0.5^x . (F) The separation distance between different CP centers (green) in *Sea2km* is higher than the theoretical distribution for random positioning (red) and unchanged with time (light vs. dark green). Two-sample Kolmogorov-Smirnov tests showed $p < 0.001$ statistical significance (marked by a star symbol) between simulation data and the control. A sliding time window of 6 hours is used throughout the figure. The results are insensitive to the length of the sliding time window. Movie 1 shows all *Sea500m* and *Sea2km* CP centers.

merical simulations (Fig. 2C).

Throughout the time series, the cloud-resolving simulation data show significantly lower average connectivity because a larger fraction of CPs has only two or three line-of-sight neighbors (see Fig. 2C inset). This result may imply the appearance of lines in high-resolution data. When inspecting Fig. 1D–E, it is qualitatively apparent that some cells form line-like structures (examples: red arrows, Fig. 1D–E). To quantify, we now introduce a *line index*, which allows us to measure the extent to which such linear structures appear more frequent than would be expected at random. The line index is defined based on local groups of CPs (solid black lines in Fig. 2A–B). For a CP to be part of a line, this CP and its neighbors must have exactly two neighbors inside the group (green points in Fig. 2A–B).

We then quantify the line index as the RCE simulations develop in time and compare the line index obtained to a randomized control (Fig. 2D). At all times, we find a significantly higher fraction of lines in the simulations than expected at random. At the intermediate stage of the simulations (days 3–8), the line index drops due to temporal clustering. If all points were located in one compact cluster, the line index would go towards zero, since in that case the cut-off distance $l = \sqrt{1/N}$ would not apply to any line-of-sight neighbors, thereby very few would have connectivity two. *Sea2km* shows a line index that is twice as large as its random counterpart, and the lines are also visible to the bare eye (see Movie 1). *Sea500m*, which constitutes a one-hour accumulated data set, hides some spatial structure and therefore has higher connectivity and a lower line index (Fig. 2C–D).

By noting the green dots in Fig. 2A that lie outside the close-up area (Fig. 2B), it is clear that most lines must be very short, and only a few are as long as the one shown in Fig. 2B. This is confirmed in Fig. 2E where we, instead of using the line index, determine the maximum length of all tracks at two specific days (see *Tracking of cold pools*). We find that the presence of long lines does not change much with simulation time.

Already from Fig. 2C–D, the spatial pattern of convective cells appears to be non-random immediately after the simulation start. To confirm this, we measure the shortest distance from one track ID to the nearest neighbor with a different track ID and do the same for a random seeding. We find that the majority of CPs are further apart than what would be expected at random (Fig. 2F). We attribute this positioning to a repulsive effect caused by the buoyancy decrease from rain-evaporation [38]. From Fig. 2F, we estimate $R_{\min} \approx 10$ km and find it to be unchanged with simulation time.

For studying the cavities (in Fig. 1), we used a sliding time window of 24 hours, while for studying the lines (in Fig. 2), we used a time window of 6 hours. In the case of the cavities, we do not want a too small time window, since that would give numerous small, noisy, cavities. For studying the lines, we do not want a too large time window, since we would then get intersecting lines

that would not be detected by the line index. Within these considerations, the results are independent of the particular choice of the time window.

By inspecting Movie 1, we note that the lines tend to grow and decay in one direction. In the following section (and in Fig. 3A–B), we suggest that this direction could be obtained by the emergence of multiple CPs along the collision line between two CPs (gray dots in Fig. 3B).

D. Circle model captures cavity and line formation

We now introduce a model consisting of growing and colliding circles, each representing a CP. Earlier, we considered the dynamics of 3-CP interactions and showed that this is a valid approximation for out-of-equilibrium diurnal cycle simulations for the current RCE setup [29]. Now, we modify the model to focus solely on 2-CP interactions. The reasoning is that in RCE, most new rain cells result from thermodynamic pre-conditioning near the gust front collision lines (Fig. 1A–B), and time delays are so long that direct forced lifting can be ruled out. In short, we initialize the model with N points randomly located within a 2D domain of size $1000 \text{ km} \times 1000 \text{ km}$ with double-periodic boundary conditions (to mimic an infinite cloud field). All points grow into circles (two highlighted in Fig. 3A) with equal and constant radial speed ($v_r \equiv 5 \text{ km h}^{-1}$). When two circle edges (the gust fronts) collide, they instantaneously create a new point (bold black dot in Fig. 3A–B), which then starts to grow at the same speed v_r . Depending on further conditions, this process either continues indefinitely, or the system eventually dies out, that is, no more circles can be generated (*Details: Mathematical model*). Initially, in each 2-CP collision, we only consider the first, unique, collision point between two circles, but later we relax this constraint.

The simplest 2-CP model includes a minimum radius, R_{\min} , that the circles need to reach to be able to replicate. Physically, CPs that are smaller than R_{\min} are too cold, hence negatively buoyant, to initialize new CPs [36, 39]. Mathematically, R_{\min} conveniently avoids singularities, that is, infinitely rapid replication. Singularities would otherwise unfold when three circle centers are located in a triangular geometry where all subsequent generations induce three new circle centers that enclose triangular areas that are progressively smaller (inset in Fig. 3B). In Fig. 3C, we present a snapshot of a simulation. We note the presence of cavities and the visual similarity with the numerical experiment results in Fig. 1D–E. In Fig. 3D, we explore the separation distance between circle centers, a distance we compare to that obtained from the numerical experiments (Fig. 2F). We find a fixed $R_{\min} = 8 \text{ km}$ to give comparable results to the experiments. We note that R_{\min} varies more strongly in the simulations than in the model. Variations in v_r both over time and between CPs can explain this.

We now also incorporate a maximum radius, R_{\max} , be-

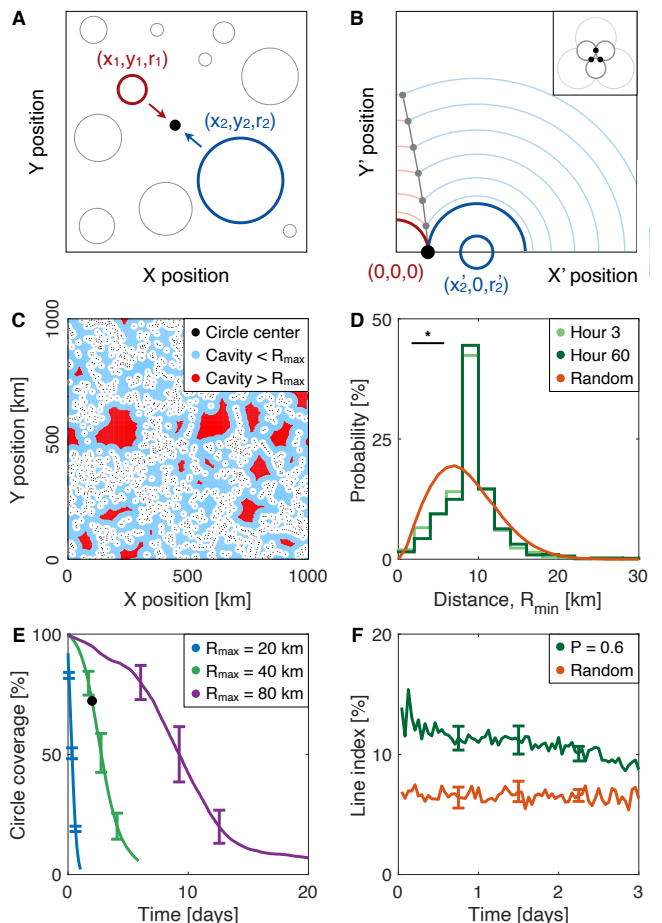


FIG. 3. Circle model captures cavity and line formation. (A) At a general time in the model, cold pools (CPs) are represented by circles of different sizes. Two circles (blue and red) will collide at the midpoint between their circles' rim if other circles do not block the midpoint (black dot). (B) To find the collision point analytically, we translate the system in such a way that the smallest circle (red) is moved to origo and reduced to zero radii. The largest circle (blue) is rotated to the X' -axis. Potential subsequent collision points (gray dots) are separated by a distance δ (for details see *Mathematical model*). The inset shows a singularity. (C) Snapshot of a simulation with $R_{\max} = 40 \text{ km}$ on day 2. The black dots are the circle centers; the white space is the area the circles enclose; the blue space is a distance less than R_{\max} away from a circle center, and the red space is further away (compare to Fig. 1D–E). (D) The separation distance between circle centers does not change with time in the model (light vs. dark green), and it is statistically different from a randomized control (two-sample Kolmogorov-Smirnov tests showed $p < 0.001$ marked by a star symbol, compare to Fig. 2F). (E) The fraction of the domain that the circles cover decays with simulation time. The smaller R_{\max} , the faster it decays. The error bars show the standard deviation for five simulation runs. The black dot shows where panel (C) is taken. (F) The line index (as defined in the caption to Fig. 2A) for $P = 0.5$ (dark green), and a control (red) (compare to Fig. 2D). All with $R_{\max} = 40 \text{ km}$. Throughout the figure, $N = 3000$, $R_{\min} = 8 \text{ km}$, and a sliding time window of 3 hours are used. Movie 2 shows a set of model simulations.

yond which the circles become passive and cannot replicate. This parameter mimics the decrease in energy and momentum as CPs grow, mix with environmental air, and lose inertia through surface drag. For simplicity, we fix R_{\min} and R_{\max} for all circles throughout a simulation. Fig. 3E shows how lowering R_{\max} results in shortening the duration of the model simulation — leading to faster cavity formation and, therefore, more rapid self-aggregation. For small R_{\max} , this model predicts a final collapse of all rain cells in the system — a feature that the numerical experiments would not develop (see also model dynamics in Movie 2).

Finally, we want to capture the formation of lines shown in Fig. 2. In Fig. 2E, we fit the length of the lines to P^x and show $P = 0.5$ in gray. Now in Fig. 3B, we suggest that a band of CPs may form along the collision curve between two CPs. In the model, we separate these new circles by a fixed distance $\delta \equiv 1$ km and let subsequent circles emerge along the curve with a probability $P = 0.5$. We find that this modification gives a line index that drops due to the overall decay of the model (Fig. 3F). However, initially, the line index is comparable to the line index found in the numerical experiments (Fig. 2D).

IV. DISCUSSION

Typical explanations for convective self-aggregation invoke circulation feedback, by which the interplay between a subsiding and a convecting region stabilizes a persistent rainy subregion [1, 40]. The current results, however, describe the path towards this final state and show that the interaction of cold pools (CPs) can explain the initial formation of cavities and their eventual growth into ever-larger cloud-free subregions. The idea that the location of CP collisions coincides with the location of new convective events is well documented [41–43]. However, to our knowledge, the suggestion that the position of CPs and their interaction may trigger self-aggregation from homogeneous conditions is new.

Here, we assume zero-wind shear conditions. Wind shear is known to induce quasi-linear geometries known as squall line convection [44–46]. Here we suggest geometric line-like structuring even in the zero wind-shear convective cloud field. The lines, we find, occur on scales of 10 km (Fig. 2E) and fewer than 10 hours (Movie 1).

The final aggregated state was repeatedly shown to be associated with an intensely convecting sub-region and a gently subsiding cloud-free environment. Studies have explored the sensitivity of the domain size to the final aggregation pattern [47, 48] and how the net short-wave and long-wave flux affects this pattern [49]. Stabilization of the final state is likely accomplished by circulation feedback, whereby divergence from the subsidence area feeds the emergent “super cold pool,” characterizing the convective sub-domain [50]. We argue here that such circulation feedback is not required for the development

of the initial cavities and their growth.

We back our analysis using a simple conceptual model based on expanding circles and their mutual interaction. We note that Torri and Kuang (2019) recently challenged the idea that CPs maintain a circular shape. While the CPs in the model expands in a perfectly circular manner, interactions with circles smaller than R_{\min} and circles that are not in the line-of-sight effectively deform the circles in the model.

Besides, we introduce two model parameters, a minimal (R_{\min}) and a maximal (R_{\max}) circle radius, and support these by the physics of CPs: we justify R_{\min} by negative buoyancy anomalies before reaching the lower radius bound, and R_{\max} by the dissipation of CP momentum when entering this upper bound. Based on simulation data, we quantify R_{\min} to be 8–12 km (Fig. 2F) and R_{\max} to be roughly two times as big (Fig. 1F).

In reality, CPs initially grow faster, and their speed of spreading decreases after a few hours (Fig. 1C) [51, 52]. However, varying the gust front expansion speed of the circles in the model is analytically challenging. Introducing this would require a circle and possibly a time-dependent speed factor in Equations 1–2. To do this, we direct the reader to the numerical approach in Haerter et al. (2019).

The presented model does not reach a final, fully-aggregated, state. This sustained activity might be obtained by adding spatial noise (displacing new circles slightly away from the exact geometric collision point) and systematically increased triggering probabilities for decreased overall rain area [53]. The final, aggregated state is then stabilized by a form of super-CP, which excites events at the edges of the supercell [50].

The merit of the current model is simplicity, but straightforward extensions could add realism: varying the time point at which the initial circles start to grow, introducing a circle specific R_{\min} and R_{\max} , adding noise on the location of new circles, and a time delay between circle collisions and the emergence of a new circle. However, to keep the model simple to convey and interpret, and intrigued by the model results presented, we decided not to implement these.

Self-aggregation, as an idealized numerical phenomenon, has recently been compared to real-world observations [54]. It is implicated in the formation of tropical cyclones [2, 3] and large-scale phenomena as the Madden-Julian Oscillation [4–6]. We here introduced a quantitative theoretical framework that, by mimicking the spatio-temporal dynamics of a population of cold pools (CPs), including their interactions, can robustly capture the spontaneous transition to convective self-aggregation.

V. MATERIALS AND METHODS

Here, we describe technical details of the cloud-resolving and large-eddy simulation setup, the tracking

of cold pool (CP) gust fronts, the tracking of cavities, as well as the definition of the mathematical model.

A. Large-eddy simulation data

We simulate the convective atmosphere using the University of California, Los Angeles (UCLA) Large Eddy Simulator with sub-grid scale turbulence parametrized after Smagorinsky [55]. We combine with a delta four-stream radiation [56] and a two-moment cloud micro-physics scheme [57]. Rain evaporation is accounted for by Seifert and Beheng (2006). Surface temperatures are set constant (Table I), and insolation is fixed using a constant equatorial zenith angle of 50° , that is, constant 650 W m^{-2} [18]. Surface heat fluxes are computed interactively and depend on the vertical temperature and humidity gradients as well as horizontal wind speed, which is approximated using the Monin-Obukhov similarity theory. Temperature and humidity are initialized using observed profiles that potentially represent convective conditions, but lose their impact after a fraction of the simulation time.

The model grid is regular in the horizontal, and periodic boundary conditions are applied in both lateral dimensions. Vertically, the model resolution varies from 100 m below 1 km, stretching to 200 m near 6 km and finally 400 m in the upper layers, and 75 vertical levels are used in all simulations except for *Sea500m*, where 63 were used (Table I). Horizontal resolution dx , domain size, and data output frequency and intervals vary (Table I). The Coriolis force and the mean wind were set to zero with weak random initial perturbations added as noise to break complete spatial symmetry. At each output time step (Table I), instantaneous surface precipitation intensity, as well as the three-dimensional moisture and velocity fields, are recorded for the entire model domain.

The computationally most extensive simulation (*Sea500m*) was carried out by Cathy Hohenegger, who kindly supplied us with several output variables of this simulation. Simulations of this type consume significant computing resources, and we, therefore, refrained from re-simulating these data. The remaining simulations were carried out by us.

Sea2km constitutes a standard setup [18], where self-aggregation sets in after approximately one week of simulation time. *Sea400m* represents a higher-resolution analog to *Sea2km*, where only a small period on a smaller domain area was simulated as a sensitivity check (*compare*: Table I). Due to the small domain size and high resolution, we do not expect this variant to aggregate but did not run the simulation long enough to affirm this. *Land2km* and *Land400m* constitute variants of *Sea2km* and *Sea400m*, where the surface latent heat fluxes are reduced to 70 % of their potential value, leading to larger cold pools.

B. Tracking of cold pools

Cold pool (CP) gust fronts are tracked similarly to the tracer particle method discussed in the recent literature [29]. In short, in any given time step particles are placed at the edges of existing precipitation cells. These particles are then advected along with the horizontal velocity field in the lowest model level ($z = 50 \text{ m}$) and settle in the gust fronts surrounding each CP.

C. Tracking of cavities

We track cavities by first setting a time window ΔT_0 , over which the pattern of precipitation cell centers is observed. A reasonable choice turns out to be $\Delta T_0 = 24$ hours, as smaller values lead to too much noise along the edges of cavities. In contrast, larger values do not correctly warrant the dynamics of cavities, i.e., growth, decay, and merging or splitting events. Our conclusions do not depend on the precise value of ΔT_0 . For all precipitation cells falling into this time window, we identify the corresponding cell centers by the use of the iterative rain cell tracking method [59]. This yields a collection of points \bar{c}_i in space, where each point $\bar{c}_i \equiv (x_i, y_i)$ is a point in the two-dimensional plane. We then scan the two-dimensional plane on the original simulation grid of 2048×2048 points. For each point \bar{c} on this grid, we evaluate the distances $d_i(\bar{c}) \equiv |\bar{c} - \bar{c}_i|$ to each cell center \bar{c}_i . The distance $d(\bar{c}) \equiv \min \{d_i(\bar{c})\}$ is then defined as the nearest distance of \bar{c} to any of the centers' \bar{c}_i .

We now define the threshold distance $d_0 \equiv 3.5 \text{ km}$. A cavity is defined as a contiguous region of points \bar{c} with $d(\bar{c}) > d_0$, that is, regions composed of points that are all located at distances greater than the threshold d_0 from existing precipitation cells. d_0 is chosen as the approximate upper limit of distance fluctuations in the aggregated sub-region of the domain. Doubling or halving this value would not have any implications for the conclusions drawn from the current study.

D. Mathematical model

N points are initialized at random locations selected uniformly on a 2D domain of size $1000 \text{ km} \times 1000 \text{ km}$. The domain has cyclic boundary conditions in both x and y directions. The N initial points are referred to as generation one. All points grow into circles with equal and constant radial speed ($v_r \equiv 5 \text{ km/h}$), hence spread isotropically in all horizontal directions. The growing circles have centers at $\bar{c}_i = [x_i, y_i]$ and increasing radii r_i . At the collision point, $[x, y]$, between two circles of generation g , a new circle belonging to the subsequent generation $g + 1$ emerges instantaneously. This collision point is determined by solving

$$(x - x_i)^2 + (y - y_i)^2 = (r_i + dr)^2, \quad (1)$$

Experiment Name	Horizontal Resolution dx [km]	Domain Size L [km]	Output Time step dt [min]	Output Interval [days]	Surface Temperature [K]	Vertical Levels
Sea2km	2	960	10	1 – 20	300	75
Land2km	2	960	10	1 – 20	300	75
Sea400m	0.4	480	10	10.07 – 10.41	300	75
Land400m	0.4	480	10	6.33 – 6.68	300	75
Sea500m	0.5	2048	60	1 – 30	301	63

TABLE I. **Summary of the numerical experiments.** The data shown indicate where the numerical experiments deviate.

and

$$(x - x_j)^2 + (y - y_j)^2 = (r_j + dr)^2, \quad (2)$$

where dr is the distance from the two circles' rim to the collision point. In the default model, only collisions that fall on the straight line between the two circle centers are allowed since that is the collision point with the highest momentum (bold black dot in Fig. 3A–B). We note this point can be found by the linear constraint

$$y = \frac{x - x_i}{x_j - x_i}(y_j - y_i) + y_i. \quad (3)$$

since this gives a set of three equations (Equations 1–3) with three unknowns (x, y, dr) , which generally has two solutions. One solution can be neglected because only the positive real solution is relevant to this model.

However, since we want the possibility to capture subsequent collisions, we stick to a more advanced approach. We translate the system to a new coordinate system where the smallest circle is moved to origo and reduced to zero radii, and the other circle is rotated onto the x' -axis (Fig. 3B). This gives two equations

$$(x')^2 + (y')^2 = (dr')^2, \quad (4)$$

and

$$(x' - x'_j)^2 + (y')^2 = (r'_j + dr')^2, \quad (5)$$

with three unknowns (x', y', dr') . If the location of the first collision point (where $y' = 0$) is not already occupied (blocked) by another circle from the same generation, then we initialize it. Theoretically, all subsequent collisions appear symmetrically in two directions away from the first collision point. However, to capture the unidirectional growth of the lines (noted in Movie 1), we only allow subsequent collision points in one direction, which we select randomly (as shown in Fig. 3B). These collision points are separated by a distance $\delta \equiv 1$ km on the y' -axis, and they emerge with a probability P under the condition that the previous collision point from the same pair of parent circles was initialized and that the location is not overtaken. We require the first collision point seeded to allow for subsequent collisions. With $R_{\min} > \delta$, that also implies that following collisions

points cannot interact with each other. Seeding all collision points ($P = 1$) in both directions with a small δ will result in a Voronoi diagram of circles [60].

Similar to the analytical approach in [29], we do not run the model strictly chronologically. To reduce simulation time, we take advantage of the fact that circles belonging to different generations cannot interact since they grow with equal and constant speed. As a result of this, we calculate all collision points for each generation before proceeding to the next generation. Generally, the last circle in any generation will initiate later than the first circle in the next generation. Therefore, when moving to the next generation, we go back in time, to the time where the first circle of the current generation was seeded.

We reduce simulation time further by not considering all possible collisions, which would be a list of $N \times (N - 1)$ collisions every generation or roughly 10^7 potential collisions for $N = 3000$. We limit this list drastically by only considering circle centers that are within a distance $2R_{\max}$ from each other. However, to run high R_{\max} , we further restrict the list by discarding circle centers whose midpoint is blocked by more than $\gamma = 30$ circles. We checked that $\gamma = 30$ is sufficiently high since increasing γ gives identical results with longer simulation time while decreasing γ did not capture all collisions.

The list of potential collision points is calculated for each generation and sorted incrementally by dr . The system is updated by inserting circles at the collision points in the order they appear. Circles are only initialized if both parent circles are larger than R_{\min} and smaller than R_{\max} and if the subsequent generation does not occupy the collision point. This process is repeated for every generation until no more collisions occur.

The mathematical model is implemented in MATLAB, and the source code is available online at <https://github.com/SilasBoyeNissen/Self-aggregation-conceptualized-by-cold-pool-organization>.

ACKNOWLEDGMENTS

We thank Steven J. Böing for useful comments and Cathy Hohenegger for discussions on her simulation results as well as for providing her RCE data. SBN acknowledges funding through the Danish National Re-

search Foundation (grant number: D NRF116). JOH gratefully acknowledges funding by a grant from the VILLUM Foundation (grant number: 13168) and the European Research Council (ERC) under the European Union’s Horizon 2020 research and innovation program (grant number: 771859). We acknowledge the Danish Climate Computing Center (DC3).

AUTHOR CONTRIBUTIONS

J.O.H. ran and processed the numerical simulations, analyzed the cavities in the simulation data, and wrote and revised the manuscript. S.B.N. analyzed the lines in the simulation data, developed, implemented, and analyzed the circle model and drafted and revised the manuscript.

COMPETING INTERESTS

The authors declare no competing interests.

-
- [1] Allison A Wing. Self-Aggregation of Deep Convection and its Implications for Climate. *Current Climate Change Reports*, 5(1):1–11, 2019. doi: <https://doi.org/10.1007/s40641-019-00120-3>.
- [2] Caroline J Muller and David M Romps. Acceleration of tropical cyclogenesis by self-aggregation feedbacks. *Proceedings of the National Academy of Sciences*, 115(12):2930–2935, 2018. doi: <https://doi.org/10.1073/pnas.1719967115>.
- [3] Allison A Wing, Suzana J Camargo, and Adam H Sobel. Role of radiative–convective feedbacks in spontaneous tropical cyclogenesis in idealized numerical simulations. *Journal of the Atmospheric Sciences*, 73(7):2633–2642, 2016. doi: <https://doi.org/10.1175/JAS-D-15-0380.1>.
- [4] Nathan P Arnold and David A Randall. Global-scale convective aggregation: Implications for the Madden-Julian Oscillation. *Journal of Advances in Modeling Earth Systems*, 7(4):1499–1518, 2015. doi: <https://doi.org/10.1002/2015MS000498>.
- [5] Masaki Satoh, Kento Aramaki, and Masahiro Sawada. Structure of tropical convective systems in aqua-planet experiments: Radiative-convective equilibrium versus the earth-like experiment. *SOLA*, 12:220–224, 2016. doi: <https://doi.org/10.2151/sola.2016-044>.
- [6] Marat F Khairoutdinov and Kerry Emanuel. Intraseasonal variability in a cloud-permitting near-global equatorial aquaplanet model. *Journal of the Atmospheric Sciences*, 75(12):4337–4355, 2018. doi: <https://doi.org/10.1175/JAS-D-18-0152.1>.
- [7] Joanne Simpson. Downdrafts as linkages in dynamic cumulus seeding effects. *Journal of Applied Meteorology*, 19(4):477–487, 1980.
- [8] Nicholas A Engerer, David J Stensrud, and Michael C Coniglio. Surface characteristics of observed cold pools. *Monthly Weather Review*, 136(12):4839–4849, 2008. doi: <https://doi.org/10.1175/2008MWR2528.1>.
- [9] David M Romps and Nadir Jeevanjee. On the sizes and lifetimes of cold pools. *Quarterly Journal of the Royal Meteorological Society*, 142(696):1517–1527, 2016. doi: <https://doi.org/10.1002/qj.2754>.
- [10] Giuseppe Torri, Zhiming Kuang, and Yang Tian. Mechanisms for convection triggering by cold pools. *Geophysical Research Letters*, 42(6):1943–1950, 2015. doi: <https://doi.org/10.1002/2015GL063227>.
- [11] Paquita Zuidema, Giuseppe Torri, Caroline Muller, and Arunchandra Chandra. A survey of precipitation-induced atmospheric cold pools over oceans and their interactions with the larger-scale environment. *Surveys in Geophysics*, pages 1–23, 2017. doi: <https://doi.org/10.1007/s10712-017-9447-x>.
- [12] Nadir Jeevanjee and David M Romps. Convective self-aggregation, cold pools, and domain size. *Geophysical Research Letters*, 40(5):994–998, 2013. doi: <https://doi.org/10.1002/grl.50204>.
- [13] Caroline Muller and Sandrine Bony. What favors convective aggregation and why? *Geophysical Research Letters*, 42(13):5626–5634, 2015. doi: <https://doi.org/10.1002/2015GL064260>.
- [14] Chris E Holloway and Steven J Woolnough. The sensitivity of convective aggregation to diabatic processes in idealized radiative-convective equilibrium simulations. *Journal of Advances in Modeling Earth Systems*, 8(1):166–195, 2016. doi: <https://doi.org/10.1002/2015MS000511>.
- [15] Cathy Hohenegger and Bjorn Stevens. Coupled radiative convective equilibrium simulations with explicit and parameterized convection. *Journal of Advances in Modeling Earth Systems*, 8(3):1468–1482, 2016. doi: <https://doi.org/10.1002/2016MS000666>.
- [16] Isaac M Held, Richard S Hemler, and V Ramaswamy. Radiative-convective equilibrium with explicit two-dimensional moist convection. *Journal of the Atmospheric Sciences*, 50(23):3909–3927, 1993.
- [17] Adrian M Tompkins and George C Craig. Radiative-convective equilibrium in a three-dimensional cloud-ensemble model. *Quarterly Journal of the Royal Meteorological Society*, 124(550):2073–2097, 1998. doi: <https://doi.org/10.1002/qj.49712455013>.
- [18] Christopher S Bretherton, Peter N Blossey, and Marat Khairoutdinov. An energy-balance analysis of deep convective self-aggregation above uniform SST. *Journal of the Atmospheric Sciences*, 62(12):4273–4292, 2005. doi: <https://doi.org/10.1175/JAS3614.1>.
- [19] Allison A Wing, Kerry Emanuel, Christopher E Holloway, and Caroline Muller. Convective self-aggregation in numerical simulations: a review. *Surveys in Geophysics*, 38(6):1173–1197, 2017. doi: <https://doi.org/10.1007/s10712-017-9408-4>.
- [20] Christopher E Holloway, Allison A Wing, Sandrine Bony, Caroline Muller, Hirohiko Masunaga, Tristan S Lecuyer,

- David D Turner, and Paquita Zuidema. Observing convective aggregation. *Surveys in Geophysics*, 38(6):1199–1236, 2017. doi:<https://doi.org/10.1007/s10712-017-9419-1>.
- [21] Marat F Khairoutdinov and Kerry A Emanuel. Aggregated convection and the regulation of tropical climate. In *29th Conference on Hurricanes and Tropical Meteorology*, Amer. Meteorol. Soc., Tucson, AZ, 2010.
- [22] Caroline J Muller and Isaac M Held. Detailed investigation of the self-aggregation of convection in cloud-resolving simulations. *Journal of the Atmospheric Sciences*, 69(8):2551–2565, 2012. doi:<https://doi.org/10.1175/JAS-D-11-0257.1>.
- [23] Adrian M Tompkins. Organization of tropical convection in low vertical wind shears: The role of cold pools. *Journal of the Atmospheric Sciences*, 58(13):1650–1672, 2001.
- [24] Wolfgang Langhans and David M Romps. The origin of water vapor rings in tropical oceanic cold pools. *Geophysical Research Letters*, 42(18):7825–7834, 2015. doi:<https://doi.org/10.1002/2015GL065623>.
- [25] Simon P de Szoeke, Eric D Skyllingstad, Paquita Zuidema, and Arunchandra S Chandra. Cold pools and their influence on the tropical marine boundary layer. *Journal of the Atmospheric Sciences*, 74(4):1149–1168, 2017. doi:<https://doi.org/10.1175/JAS-D-16-0264.1>.
- [26] Franziska Glassmeier and Graham Feingold. Network approach to patterns in stratocumulus clouds. *Proceedings of the National Academy of Sciences*, 114(40):10578–10583, 2017. doi:<https://doi.org/10.1073/pnas.1706495114>.
- [27] Carlo Cafaro and Gabriel G Rooney. Characteristics of colliding density currents: A numerical and theoretical study. *Quarterly Journal of the Royal Meteorological Society*, 144(715):1761–1771, 2018. doi:<https://doi.org/10.1002/qj.3337>.
- [28] Steven J Böing. An object-based model for convective cold pool dynamics. *Mathematics of Climate and Weather Forecasting*, 2(1), 2016. doi:<https://doi.org/10.1515/mcwf-2016-0003>.
- [29] Jan O Haerter, Steven J Böing, Olga Henneberg, and Silas Boye Nissen. Circling in on convective organization. *Geophysical Research Letters*, 46(12):7024–7034, 2019. doi:<https://doi.org/10.1029/2019GL082092>.
- [30] Jean-Yves Grandpeix and Jean-Philippe Lafore. A density current parameterization coupled with Emanuel’s convection scheme. Part I: The models. *Journal of the Atmospheric Sciences*, 67(4):881–897, 2010. doi:<https://doi.org/10.1175/2009JAS3044.1>.
- [31] Peter G Black. Mesoscale cloud patterns revealed by apollo-soyuz photographs. *Bulletin of the American Meteorological Society*, 59(11):1409–1419, 1978.
- [32] Paquita Zuidema, Zhujun Li, Reginald J Hill, Ludovic Bariteau, Bob Rilling, Chris Fairall, W Alan Brewer, Bruce Albrecht, and Jeff Hare. On trade wind cumulus cold pools. *Journal of the Atmospheric Sciences*, 69(1):258–280, 2012. doi:<https://doi.org/10.1175/JAS-D-11-0143.1>.
- [33] Zhe Feng, Samson Hagos, Angela K Rowe, Casey D Burleyson, Matus N Martini, and Simon P Szoeke. Mechanisms of convective cloud organization by cold pools over tropical warm ocean during the amie/dynamo field campaign. *Journal of Advances in Modeling Earth Systems*, 7(2):357–381, 2015. doi:<https://doi.org/10.1002/2014MS000384>.
- [34] Christopher S Bretherton and Marat F Khairoutdinov. Convective self-aggregation feedbacks in near-global cloud-resolving simulations of an aquaplanet. *Journal of Advances in Modeling Earth Systems*, 7(4):1765–1787, 2015. doi:<https://doi.org/10.1002/2015MS000499>.
- [35] Nadir Jeevanjee and David M Romps. Effective buoyancy, inertial pressure, and the mechanical generation of boundary layer mass flux by cold pools. *Journal of the Atmospheric Sciences*, 72(8):3199–3213, 2015. doi:<https://doi.org/10.1175/JAS-D-14-0349.1>.
- [36] Marielle B Fournier and Jan O Haerter. Tracking the gust fronts of convective cold pools. *Journal of Geophysical Research: Atmospheres*, 124(21):11103–11117, 2019. doi:<https://doi.org/10.1029/2019JD030980>.
- [37] David W Matula and Robert R Sokal. Properties of Gabriel graphs relevant to geographic variation research and the clustering of points in the plane. *Geographical Analysis*, 12(3):205–222, 1980. doi:<https://doi.org/10.1111/j.1538-4632.1980.tb00031.x>.
- [38] Adrian M Tompkins and Addisu G Semie. Organization of tropical convection in low vertical wind shears: Role of updraft entrainment. *Journal of Advances in Modeling Earth Systems*, 9(2):1046–1068, 2017. doi:<https://doi.org/10.1002/2016MS000802>.
- [39] Aryeh J Drager and Susan C van den Heever. Characterizing convective cold pools. *Journal of Advances in Modeling Earth Systems*, 9(2):1091–1115, 2017. doi:<https://doi.org/10.1002/2016MS000788>.
- [40] Allison A Wing and Kerry A Emanuel. Physical mechanisms controlling self-aggregation of convection in idealized numerical modeling simulations. *Journal of Advances in Modeling Earth Systems*, 6(1):59–74, 2014. doi:<https://doi.org/10.1002/2013MS000269>.
- [41] James FW Purdom. Some uses of high-resolution goes imagery in the mesoscale forecasting of convection and its behavior. *Monthly Weather Review*, 104(12):1474–1483, 1976.
- [42] John F Weaver and Stephan P Nelson. Multiscale aspects of thunderstorm gust fronts and their effects on subsequent storm development. *Monthly Weather Review*, 110(7):707–718, 1982.
- [43] Giuseppe Torri and Zhiming Kuang. On Cold Pool Collisions in Tropical Boundary Layers. *Geophysical Research Letters*, 46(1):399–407, 2019. doi:<https://doi.org/10.1029/2018GL080501>.
- [44] Richard Rotunno, Joseph B Klemp, and Morris L Weisman. A Theory for Strong, Long-Lived Squall Lines. *Journal of the Atmospheric Sciences*, 45(3):463–485, 1988.
- [45] Morris L Weisman and Richard Rotunno. a theory for strong long-lived squall lines revisited. *Journal of the Atmospheric Sciences*, 61(4):361–382, 2004.
- [46] ZJ Lebo and H Morrison. Effects of horizontal and vertical grid spacing on mixing in simulated squall lines and implications for convective strength and structure. *Monthly Weather Review*, 143(11):4355–4375, 2015. doi:<https://doi.org/10.1175/MWR-D-15-0154.1>.
- [47] Nathan P Arnold and William M Putman. Non-rotating Convective Self-Aggregation in a Limited Area AGCM. *Journal of Advances in Modeling Earth Systems*, 10(4):1029–1046, 2018. doi:<https://doi.org/10.1002/2017MS001218>.

- [48] Casey R Patrizio and David A Randall. Sensitivity of Convective Self-Aggregation to Domain Size. *Journal of Advances in Modeling Earth Systems*, 11(7):1995–2019, 2019. doi:<https://doi.org/10.1029/2019MS001672>.
- [49] Tom Beucler and Timothy Cronin. A budget for the size of convective self-aggregation. *Quarterly Journal of the Royal Meteorological Society*, 145(720):947–966, 2019. doi:<https://doi.org/10.1002/qj.3468>.
- [50] JM Windmiller and Cathy Hohenegger. Convection on the edge. *Journal of Advances in Modeling Earth Systems*, 2019. doi:<https://doi.org/10.1029/2019MS001820>.
- [51] Leah D Grant and Susan C van den Heever. Cold pool dissipation. *Journal of Geophysical Research: Atmospheres*, 121(3):1138–1155, 2016. doi:<https://doi.org/10.1002/2015JD023813>.
- [52] Leah D Grant and Susan C van den Heever. Cold Pool-Land Surface Interactions in a Dry Continental Environment. *Journal of Advances in Modeling Earth Systems*, 10(7):1513–1526, 2018. doi:<https://doi.org/10.1029/2018MS001323>.
- [53] Jan O Haerter. Convective Self-Aggregation As a Cold Pool-Driven Critical Phenomenon. *Geophysical Research Letters*, 46(7):4017–4028, 2019. doi:<https://doi.org/10.1029/2018GL081817>.
- [54] Tom Beucler, Tristan H Abbott, Timothy W Cronin, and Michael S Pritchard. Comparing Convective Self-Aggregation in Idealized Models to Observed Moist Static Energy Variability near the Equator. *Geophysical Research Letters*, 46(17–18):10589–10598, 2019. doi:<https://doi.org/10.1029/2019GL084130>.
- [55] Joseph Smagorinsky. General circulation experiments with the primitive equations: I. the basic experiment. *Monthly weather review*, 91(3):99–164, 1963.
- [56] Robert Pincus and Bjorn Stevens. Monte Carlo spectral integration: A consistent approximation for radiative transfer in large eddy simulations. *Journal of Advances in Modeling Earth Systems*, 1(2):1–9, 2009. doi:<https://doi.org/10.3894/JAMES.2009.1.1>.
- [57] Bjorn Stevens, Chin-Hoh Moeng, Andrew S Ackerman, Christopher S Bretherton, Andreas Chlond, Stephan de Roode, James Edwards, Jean-Christophe Golaz, Hongli Jiang, Marat Khairoutdinov, Michael P. Kirkpatrick, David C. Lewellen, Adrian Lock, Frank Miller, David E. Stevens, Eoin Whelan, and Ping Zhu. Evaluation of large-eddy simulations via observations of nocturnal marine stratocumulus. *Monthly Weather Review*, 133(6):1443–1462, 2005. doi:<https://doi.org/10.1175/MWR2930.1>.
- [58] A Seifert and KD Beheng. A two-moment cloud microphysics parameterization for mixed-phase clouds. Part 1: Model description. *Meteorology and Atmospheric Physics*, 92(1-2):45–66, 2006. doi:<https://doi.org/10.1007/s00703-005-0113-3>.
- [59] Christopher Moseley, Peter Berg, and Jan O Haerter. Probing the precipitation life cycle by iterative rain cell tracking. *Journal of Geophysical Research: Atmospheres*, 118(24):13–361, 2013. doi:<https://doi.org/10.1002/2013JD020868>.
- [60] Deok-Soo Kim, Donguk Kim, and Kokichi Sugihara. Voronoi diagram of a circle set from Voronoi diagram of a point set: II. Geometry. *Computer Aided Geometric Design*, 18(6):563–585, 2001. doi:[https://doi.org/10.1016/S0167-8396\(01\)00051-6](https://doi.org/10.1016/S0167-8396(01)00051-6).

SUPPLEMENTARY INFORMATION

In the supplement, we analytically find the average number of line-of-sight neighbors in a system with randomly positioned cells (Fig. S1), we follow the development of the cavities in Fig. 1D–E over a longer time (Fig. S2), we explore the updraft speed distribution functions in the numerical experiments (Fig. S3), and we study the cavity size evolution and distribution in *Sea2km* and *Sea500m* (Fig. S4). Besides, we include a movie of *Sea500m* and *Sea2km* showing the cold pool centers throughout the simulations (Movie 1) and a movie of various simulations created with the circle model (Movie 2).

Line-of-sight collisions for random seeding

Consider N points randomly seeded in a total area $A = \pi R^2$. A line-of-sight connection (also known as a Gabriel connection) between any two points i and j at distance r exists if there are no further points located within the circle of radius $r/2$ centered at $(\bar{c}_i + \bar{c}_j)/2$, which contains i and j (Fig. S1). One must further consider the probability of finding two points at distance r . For this purpose, define the density of points as $\rho \equiv N/A = N/\pi R^2$. Now consider the tiny area $a(r)dr$, which is the area enclosed by two circles of radii r and $r + dr$. The number of points contained in this area is

$$n(r)dr = \rho a(r) \approx \frac{2Nr}{R^2} dr. \quad (\text{S1})$$

For any two points at a given distance r , we now consider the probability $p(r)$, that none of the remaining $N - 2$ points lie within the circle of radius $r/2$:

$$P(r) = P_0^{N-2} = \left(1 - \frac{\pi(r/2)^2}{\pi R^2}\right)^{N-2}, \quad (\text{S2})$$

where

$$P_0 = 1 - \frac{\pi(r/2)^2}{\pi R^2} \quad (\text{S3})$$

is the probability that any single point is not inside the area enclosed by a circle of radius $r/2$. Now the total number of expected line-of-sight connections for a fixed given point to any of the other points can be computed:

$$N_{\text{LOS}} = \int_0^R dr n(r)P(r) \quad (\text{S4})$$

$$= \int_0^R dr \frac{2Nr}{R^2} \left(1 - \frac{r^2}{4R^2}\right)^{N-2} \quad (\text{S5})$$

$$= \frac{4(1 - (\frac{3}{4})^{N-1})}{1 - N^{-1}}, \quad (\text{S6})$$

which gives $\lim_{N \rightarrow \infty} N_{\text{LOS}} = 4$. Hence, when repeating for all N and avoiding double-counting of connections, one obtains that there are $2N$ line-of-sight connections.

Movie 1: Simulation cold pool centers

All cold pool (CP) centers in **(A)** *Sea500m* and **(B)** *Sea2km* illustrated with a sliding time window of 6 hours. The first CPs appear 35 hours later in *Sea500m* compared to *Sea2km*. The spatial domain of *Sea500m* is slightly bigger than *Sea2km* (see *Simulation data*). Each color indicates a unique track (see *Tracking of cold pools*). The black box in *Sea2km* at 240–245 hours shows the subset illustrated in Fig. 2A. Note the formation of cavities and the appearance of lines of length up to ~ 10 km.

Movie 2: Model circle centers

All circle centers in four different model simulations. **(A)** $R_{\text{max}} = 20$ km and $P = 0$. **(B)** $R_{\text{max}} = 40$ km and $P = 0$. **(C)** $R_{\text{max}} = 80$ km and $P = 0$. **(D)** $R_{\text{max}} = 40$ km and $P = 0.5$. In all four simulations $N = 3000$, $R_{\text{min}} = 8$ km, the sliding time window is 3 hours, and the initial seedings are identical. The color scheme is similar to Fig. 3E. We note that cavities form the fastest when R_{max} is small (panel A). Generally, cavity formation results in model collapse (see also Fig. 3E). Panel B at time 47–49 hours is identical to Fig. 3C. In panel D, we note the formation of short lines.

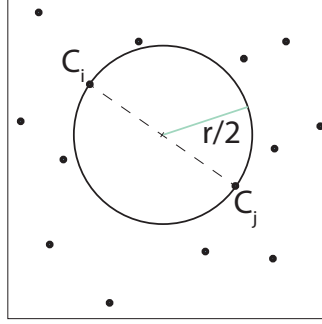


FIG. S1. **Line-of-sight connection.** Schematic illustrating points in a two-dimensional domain and highlighting two particular points \bar{c}_i and \bar{c}_j at distance r that have a line-of-sight connection. The circle of radius $r/2$, including the two points \bar{c}_i and \bar{c}_j , highlights the line-of-sight condition, namely, that no other points must be contained within the circle shown.

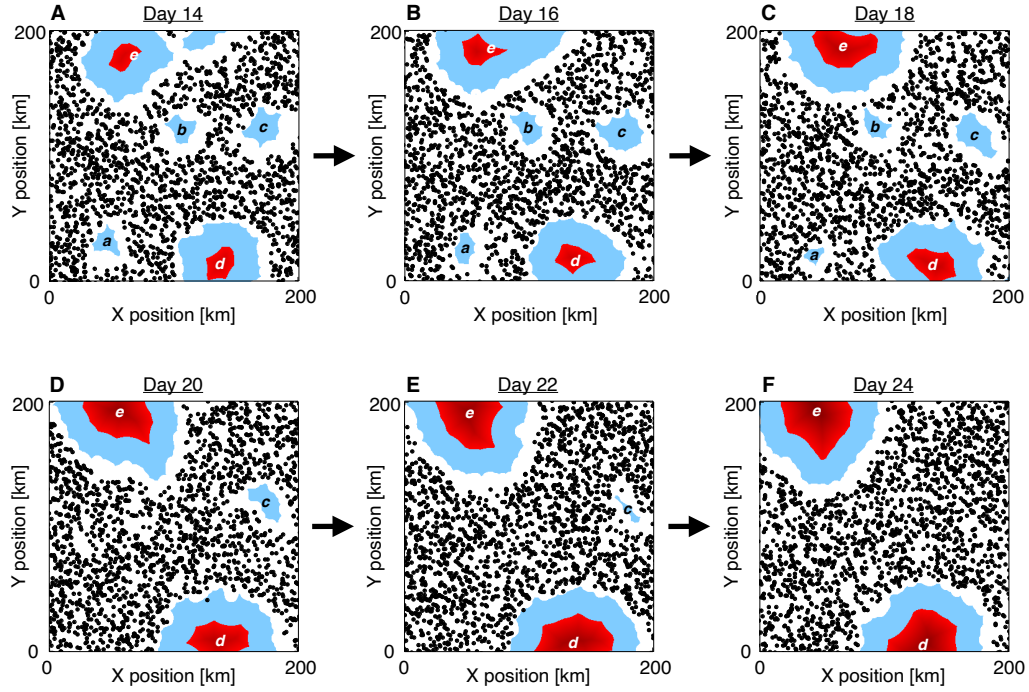


FIG. S2. **Patterns of cells at various times during self-aggregation.** Panel (A) and (F) are identical to Fig. 1D–E.

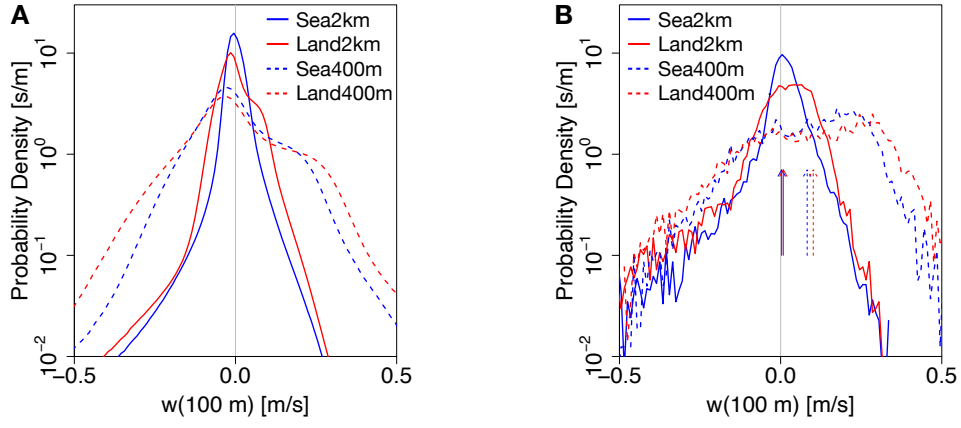


FIG. S3. **Updraft speed distribution functions.** (A) Histograms showing the updraft speed for the two different horizontal resolutions. Note the broader distribution for the higher model resolution. (B) Analogous to (A), but conditioning on locations with tracked CP gust fronts. Note the skewness for both resolutions, but the overall positive bias for the higher resolution, but not for the lower (the arrows mark the respective average values). This indicates that convergence is weak and challenging to track precisely for the coarser-resolution case.

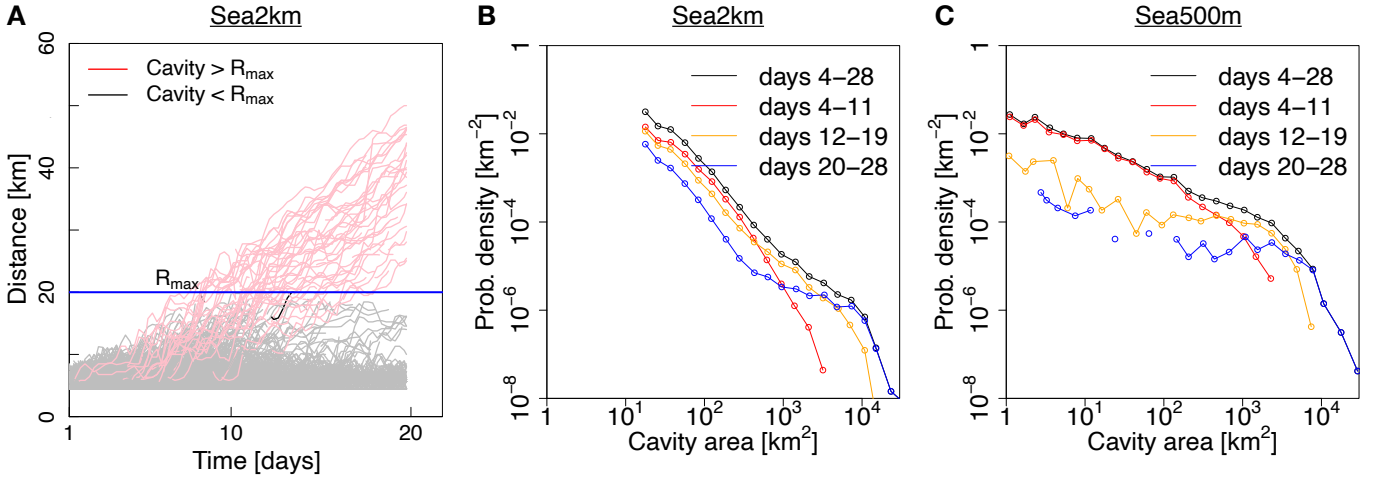


FIG. S4. **Cavity size evolution and distribution.** (A) Cavity size evolution for *Sea2km*. (B) Distribution functions of cavity area for different periods within the *Sea2km* sea surface simulation, that is, the one showing self-aggregation. (C) Analogous to (B) but for *Sea500m*.